ON THE IMPACT OF CALCAREOUS BIOFOULING ON TURBULENT BOUNDARY LAYERS

Ioannis K. Kaminaris, Elias Balaras,
Department of Mechanical and Aerospace Engineering
The George Washington University
Washington, DC, USA
kaminaris@gwu.edu; balaras@gwu.edu

Vidya Vishwanathan and Michael P. Schultz
United States Naval Academy
Annapolis, MD, USA
vishwana@usna.edu; mschultz@usna.edu

ABSTRACT

The impact of biofouled topographies on the mean flow statistics is studied via direct numerical simulations (DNS) of spatially developing turbulent boundary layers, validated by peer experimental studies. Barnacle- and tubeworm-type topographies are employed as study cases at a fixed planar solidity, λ_p, of 17% and at two different frontal solidities, λ_f, of approximately 8.3% and 6.5%. Surfaces are synthesized via our in-house Python object oriented algorithm, *AdRoS*, in order to mimic actual biofouled topographies. The effect of the frontal solidity is investigated by performing a parametric study where only the latter is altered while the rest of the topographical statistics are kept the same. Strong correlation is observed between the frontal solidity and the roughness function, ΔU^+, as well as the boundary layer growth rate, however that correlation was found to be more dominant in the barnacle-type topographies. Significant flow separation has been observed in all topographies, while barnacle-type topographies showed an increased inclination towards flow separation due to their spatial development.

Introduction

When the hull of a naval vessel is submerged in sea water it is exposed to marine biofouling resulting in increased hydrodynamic resistance. Schultz *et al.* (2011) reported that the total cost associated with biofouling for just the DDG-51 vessel class of the US Navy can rise up to $1B over a period of 15 years. The corresponding shaft power can increase by up to 86%, compared to a hydraulically smooth hull (see Schultz, 2007). So far multiple studies have focused on the interaction of wall-roughness with turbulent boundary layers, but only few of them targeted specifically biofouling-type roughness and their impact on the hydrodynamic drag. Analyses of scanned biofouled surfaces indicate that such roughness is in the high skewness ($Sk > 1$) and low effective slope ($ES < 0.5$) regime (see Dehn *et al.* (2017)). Monty *et al.* (2016) reported experiments of zero pressure gradient turbulent boundary layers over light calcareous fouling (tubeworms) plates synthesised using repeated tiles of scanned surfaces. Using scaling arguments they indicated that in cruise conditions this sparse tubeworm fouling can cause up to 23% increase in total resistance (and hence the required shaft power) for a $124m$ long frigate type geometry, and upwards of a 34% increase for a very large crude carrier. More recently, barnacle-type topographies were studied by Kaminaris *et al.* (2023*b*) using DNS in a boundary layer configuration. They reported that the pressure force on the roughness has the highest contribution to the total drag (up to $\approx 88\%$). In a study with similar rough surfaces Sarakinos & Busse (2022) performed DNS of turbulent channel flows over barnacle-type topographies with light clustering and concluded that the frontal solidity, λ_f, has the highest impact on the roughness function for low planar solidity, λ_p, surfaces.

The primary goal of this work is to investigate how the frontal solidity of rough surfaces similar to the those found on naval vessels impacts the mean flow and the resulting skin friction, as well as to assess its effect when different organism-type surfaces are considered. We use a library of topographies populated by barnacles and tubeworms, where the frontal solidity is systematically changed, to perform DNS. Emphasis is given to the impact of the surface statistics to the roughness function, ΔU^+, the evolution of the boundary layer and the flow separation which takes place in the vicinity the individual organisms.

Methodologies and parametric space

In the present study monoculture-type topographies of barnacle- and tubeworm-type are utilized, which are generated by our in-house synthesis algorithm, *AdRoS*. A top view of the topographical arrangements can be found in Figure 1. For both the two different organism-type topographies the planar solidity considered is $\lambda_p = 17\%$. The computational domain has dimensions of $75\delta_{LE} \times 14\delta_{LE}$, in the streamwise (x) and spanwise (z) directions respectively (δ_{LE} is the incoming boundary layer thickness at the leading-edge of the roughness) and the freestream boundary is positioned $10\delta_{LE}$ from the wall. The blockage-ratio range for the case of the BR17-$\lambda_{f,max}$ topography is $9 \leq \delta/\hbar_B \leq 18$, while of the TR17-$\lambda_{f,max}$ topography is $21 \leq \delta/\hbar_T \leq 32$, where $\hbar_B$ and $\hbar_T$ are the characteristic heights of the barnacles and tube-
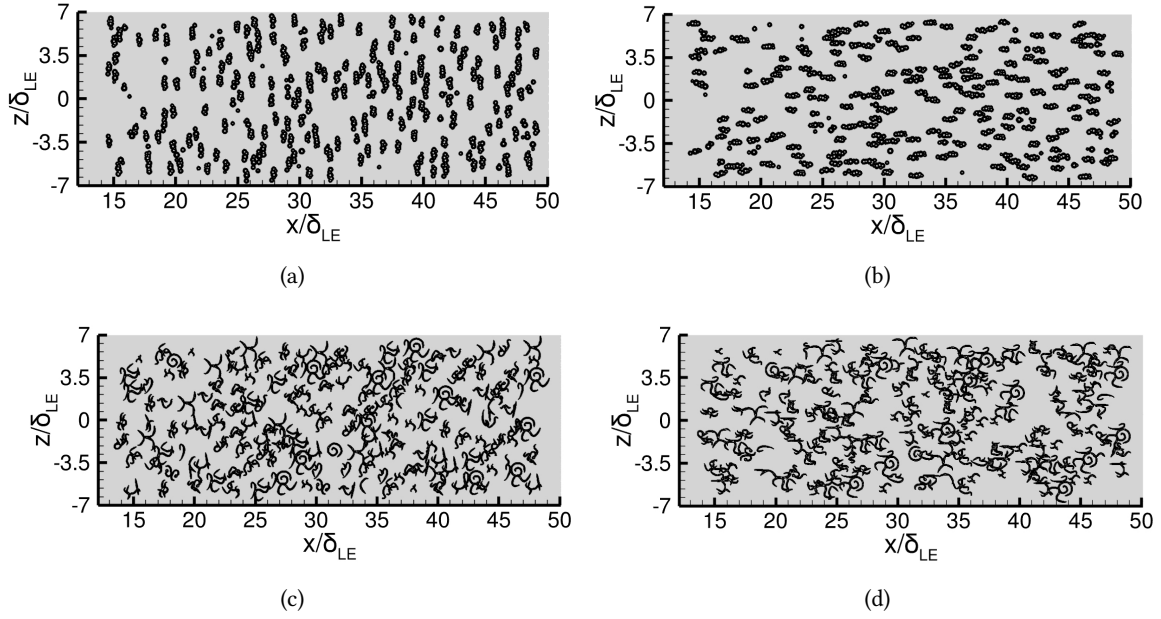
(a)

(b)

(c)

(d)

Figure 1: Synthesized monoculture-type biofouling topographies at $\lambda_p = 17\%$. Barnacle-type topographies at a) $\lambda_f = 8.3\%$ ($\lambda_{f,max}$) and b) $\lambda_f = 6.69\%$ ($\lambda_{f,min}$); Tubeworm-type topographies at c) $\lambda_f = 8.28\%$ ($\lambda_{f,max}$) and d) $\lambda_f = 6.43\%$ ($\lambda_{f,min}$).

Topography	λ_p (%)	λ_f (%)	$\overline{h}/\delta_{LE}$	$\hbar/\delta_{LE}$	σ/δ_{LE}	Skewness (Sk)	Kurtosis (Ku)	Effective Slope (ES_{xz})	k_s/δ_{LE}	Symbols
BR17-$\lambda_{f,max}$	17.8	8.3	0.0230	0.1120	0.057	2.537	8.316	0.147	0.497	●
BR17-$\lambda_{f,min}$	17.6	6.69	0.0228	0.1120	0.057	2.556	8.411	0.144	0.092	○
TR17-$\lambda_{f,max}$	17.5	8.28	0.0100	0.0474	0.0240	2.323	6.971	0.138	0.140	▲
TR17-$\lambda_{f,min}$	17.3	6.43	0.0098	0.0474	0.0240	2.337	7.031	0.136	0.087	△

Table 1: Parametric space considered for the barnacle- and tubeworm-type topographies.

worms, respectively. The inflow boundary is positioned upstream of the rough area to allow the boundary layer to develop first. The Reynolds number at the inflow plane is set to $Re_\theta = U_e\theta_o/\nu = 1600$ ($\theta_o = 0.16D$ is the momentum thickness at the inflow plane, U_e the freestream velocity and ν the kinematic viscosity of the fluid). The highest friction Reynolds number range acquired for the rough-wall part of the domain is estimated as $1700 \leq Re_\tau \leq 2870$. The computational domain is discretized using $4200 \times 1200 \times 350$ grid points in the streamwise (x), spanwise (z) and wall-normal (y) directions respectively in the case of the barnacle-type topographies which resulted in a resolution of $\Delta x^+ = 10.5$, $\Delta z^+ = 9$ and $\Delta y^+ = 0.9$ (based on the average friction velocity for the smooth part of the plate), while in the case of the smaller size tubeworms the computational domain is refined and thus discretized using $7200 \times 1800 \times 370$ grid points, resulting in $\Delta x^+ = 6.5$, $\Delta z^+ = 6$ and $\Delta y^+ = 0.7$.

An in-house, finite-difference, Navier–Stokes solver is employed for all cases presented in this work. For the time advancement a semi-implicit method is employed, where all terms are treated explicitly using the Runge–Kutta third-order scheme, except for the viscous and convective terms in the wall-normal direction which are treated implicitly using a second-order Crank–Nicholson scheme. All spatial derivatives are discretised using second-order central-differences on a staggered grid. The code is parallelised using a classical domain decomposition approach. The computational domain is descretized using a Cartesian grid and the rough-
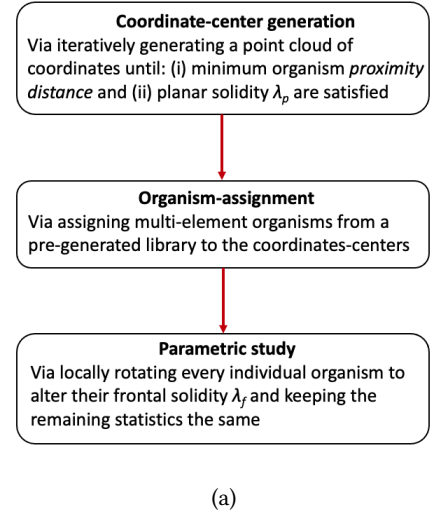

(a)

Figure 2: Structure of the surface synthesis algorithm, *AdRoS*.

ness elements are represented via a direct-forcing, immersed-boundary method. The details on the overall formulation can be found in Yang & Balaras (2006).

The surface synthesis algorithm can briefly be described in three main steps (see Figure 2): i) the generation of xy co-

ordinates of the organisms centres via an iterative process by using uniform-probability density functions; at that stage the targeted planar solidity, as well as the organism proximity distance are given as inputs; ii) the organism-shape assignment from a pre-designed designed library, iii) the parametric study. In the present work the parametric study is performed with respect to the frontal solidity parameter, λ_f, which is computed as follows:

$$\lambda_f = \frac{S_f}{S_o} 100\%,$$

$$S_f = \begin{cases} \oiint\limits_{S} \hat{n}_u \cdot d\vec{S}, & \hat{n}_u \cdot \hat{n}_s < 0 \\ 0, & \hat{n}_u \cdot \hat{n}_s \geq 0 \end{cases}, \quad \hat{n}_s = \frac{\vec{S}}{\left\| \vec{S} \right\|} \qquad (1)$$

where $\hat{n}_s$ is the unit normal vector of a rough surface and $\hat{n}_u$ the unit vector in the direction of the mean flow (i.e. x-direction). Moreover, the planar solidity (or coverage), λ_f, can be computed as:

$$\lambda_p = \frac{S_p}{S_o} 100\%,$$

$$S_o = \oiint\limits_{S} \hat{n}_o \cdot d\vec{S}, \quad S_p = \oiint\limits_{S} \hat{n}_o \cdot d\vec{S}_{h>0} \qquad (2)$$

where $\hat{n}_o$ is defined as the unit normal vector of a smooth surface and $\vec{S}$ the normal area vector of a rough surface.

Results

The validation of the DNS setup can be found in Kaminaris *et al.* (2023*b*) where detailed comparisons have been made against the experimental results reported in Womack *et al.* (2022) for barnacle covered topographies. The same study was also used as a guide for the current grid design and the size of the statistical sample. The ratio of the Kolmogorov length scale to the local cell-size ranges between $2 < \Delta x/\eta < 6$, which is in the range of DNS reported in the literature. A time sample of, ~ 70 eddy-turnover times based on δ/U_e, was found sufficient to obtain converged statistics for the velocity field given that additional averaging is performed in the spanwise direction.

In Figure 3 the streamwise evolution of the boundary layer (δ/δ_{LE}) and momentum thickness (θ/δ_{LE}) are presented together with the evolution of the friction velocity (u_τ/U_e) over the full extent of the rough-wall boundary layer for the topographies shown in Figure 1 with surface statistics reported in Table 1. It can be seen that the frontal solidity clearly affects the growth of the boundary layer in both the barnacle- and tubeworm-type topographies, with increasing λ_f resulting in increased δ/δ_{LE}. However, the effect seems to be more evident in the barnacle-type topographies, where the average difference between the high and low frontal solidity cases is approximately 20%, compared to 6% in the tubeworm-type topographies. The same trends and approximately the same average difference can be detected in the case of the momentum thickness evolution as well. With regard to friction velocity evolution the effect of the frontal solidity seems to be substantial in only the BR17 cases, while in the TR17 cases the effect seems to be mitigated. Overall, the weaker impact of λ_f to the boundary layer growth over the tubeworm-type topographies is probably due to fact that the shape of
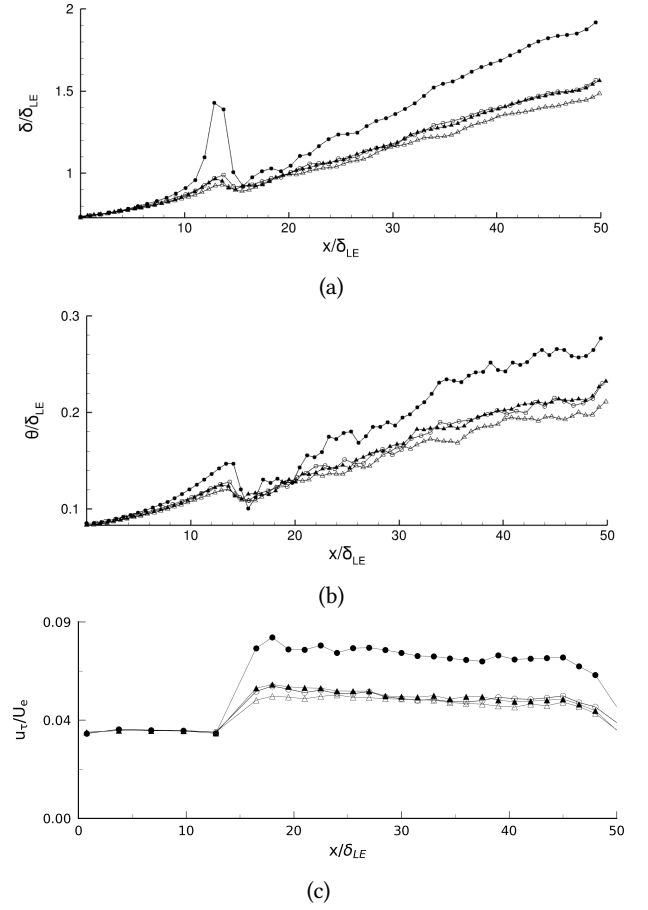

(a)

(b)

(c)

Figure 3: Streamwise evolution of the a) boundary layer thickness, δ/δ_{LE}, b) momentum thickness, θ/δ_{LE} and c) friction velocity (u_τ/U_e). Symbols from Table 1.
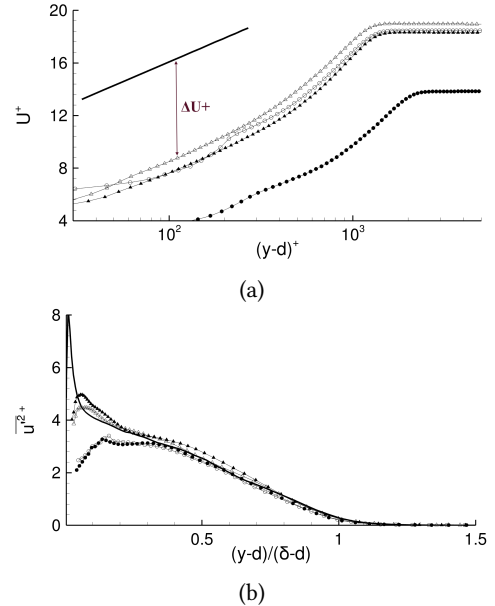

(a)

(b)

Figure 4: a) Mean streamwise velocity profiles in inner coordinates; b) streamwise Reynolds stress profiles in outer coordinates for the topographies shown in Figure 1 at x/δ_{LE}=35. Symbols from Table 1. Solid black line indicates the smooth wall at a similar friction Reynolds number; $\frac{1}{\kappa}\ln y^+ + B$, $\kappa = 0.384$ and $B = 4.2$. Shown in red is the roughness function, ΔU^+.
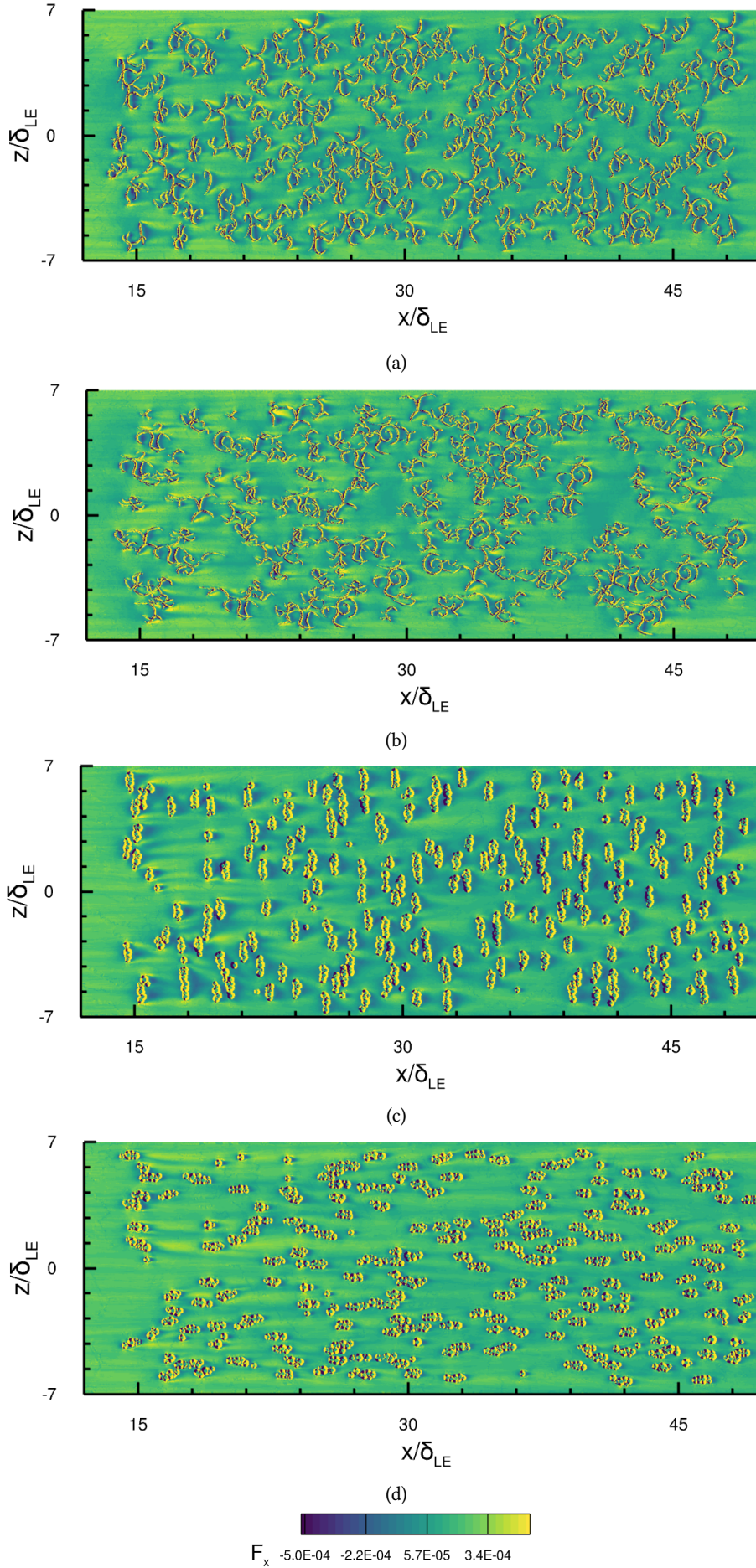
F_x -5.0E-04   -2.2E-04   5.7E-05   3.4E-04

Figure 5: Distribution of total streamwise force for the a) TR17-$\lambda_{f,max}$, b) TR17-$\lambda_{f,min}$, c) BR17-$\lambda_{f,max}$ and d) BR17-$\lambda_{f,min}$ topographies.
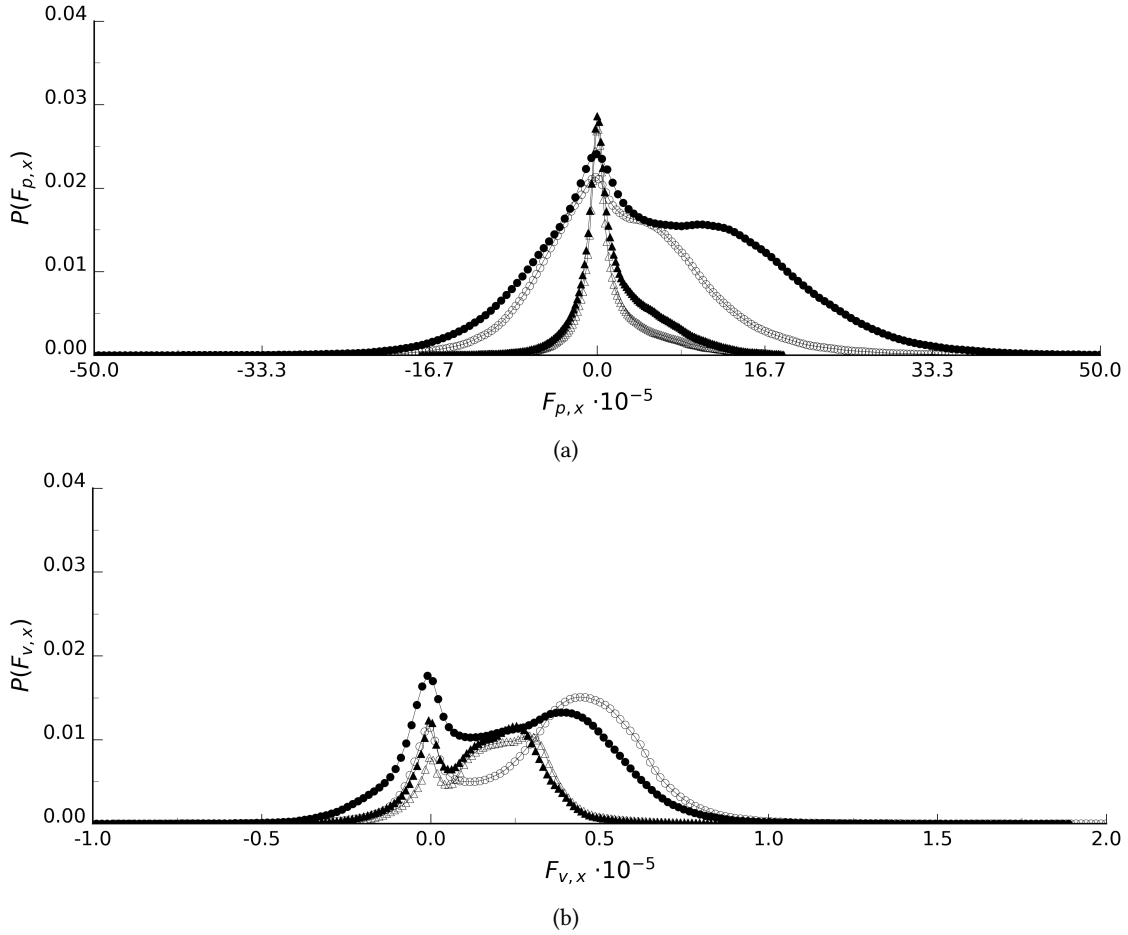
4

(a)

(b)

Figure 6: Probability density functions of the a) pressure and b) viscous forces for the topographies shown in Figure 1. Symbols from Table 1.

the tubeworm-type organisms is significantly more elongated and thus tends to spread out more by flooding the whole flat surface. In this way there are always some forefront individual tubeworm organisms that act as a shield for the ones that come next, which therefore cannot contribute to drag as much as the more concentrated barnacle-type topographies. Besides the spatial distribution of the organisms, the observed difference regarding the frontal solidity impact to the boundary layer between the barnacle- and tubeworm-type topographies may lay also on the fact that the topographies greatly differ in the organism-characteristic height, $\hbar$, which is $\hbar_B \approx 2.5 \, \hbar_T$. This is also supported by the findings of Kaminaris $et\ al.$ (2023a), where a lower λ_f barnacle-type topography found to result in a higher ΔU^+ compared to a lower $\hbar$ tubeworm-type topography of the same planar solidity, λ_p.

The effect of the frontal solidity on the mean flow for both the barnacle and tubeworm-type topographies can be seen in Figure 4a, where the mean streamwise velocity is presented in inner coordinates. Here, the zero-plane displacement, d, is subtracted from the wall-normal coordinate to allow for the wall-origin correction due to the existence of the roughness. In the present study d is iteratively estimated as a fitting parameter which allows for the slope of the rough-wall log-layer to match the well-known one of the smooth-wall. It can be easily seen that the trends observed for the boundary layer evolution hold for the mean velocity as well. Once more, the highest impact of the roughness to the mean flow occurs in the BR17-$\lambda_{f,max}$ case. The roughness impact on the mean velocity is represented by a vertical shift of the loga-

rithmic layer from the smooth-wall reference, namely ΔU^+. Thus, Figure 4a suggests that increased λ_f results in increased ΔU^+, which is on par with findings from previous studies in similar planar solidities (see Womack $et\ al.$, 2022; Sarakinos & Busse, 2022; MacDonald $et\ al.$, 2016, for details). Moreover, the outer-layer similarity is verified and demonstrated in Figure 4b via the collapse of the streamwise Reynolds stresses for all rough topographies studied alongside the respective one of a smooth-wall at approximately the same Re_τ, while the small discrepancies between the rough and smooth Reynolds stress profiles could be due to small time-sample differences of the various simulations.

The streamwise force distributions, F_x, for all topographies studied in the present are shown in Figure 5. The details of the force computation can be found in Kaminaris $et\ al.$ (2023b). From the contours of Figure 5 it can be readily seen that both the barnacle- and tubeworm-type topographies impose a significant footprint in the streamwise force map, with the former creating a more homogeneous pattern and the latter a more polarized one. This is expected, as it was discussed above for the boundary-layer evolution, due to both the differences in the organism shape/distribution as well the characteristic height. Strong flow separation is detected at the lateral and leeward sides of both barnacle- and tubeworm-type organisms, with the effects to be more evident in the case of the barnacle-type. In order to more qualitatively assess the differences in the force distributions between all the surfaces studied herein, their probability density functions, pdf, are plotted in Figure 6.

The streamwise pressure force probability density function, $P(F_{p,x})$, is presented in Figure 6a and shows a clear difference in the force spectrum range between the barnacle- and tubeworm-type topographies with the former exhibiting the wider range. This is attributed to the fact that the tubeworm-type organisms, as discussed above, due to their shape flood the whole plate and thus create a more uniformly distributed topography allowing for less extreme force values to arise. Furthermore, the distributions' peak near zero is an indication of flow separation, while the slightly increased $P(F_{p,x})$ values of zero pressure forces in the tubeworm-type topographies is attributed to the significantly larger planar size of the individual tubeworm organisms which acts as a low-momentum shelter. With respect to the $\lambda_{f,max/min}$ impact to the force distributions, one can observe that similar shape distributions of different magnitude are formed for same type organisms, as well as that the higher frontal solidity cases result in higher $P(F_{p,x})$ values, which is expected since the vertical alignment of the organisms relative to the dominant flow direction imposes more drag. The latter is valid for both barnacle- and tubeworm-type topographies. It is also noted that in the case of the tubeworm-type topographies the distributions are overall fairly similar, as expected from the observations made in Figures 3, 4.

The streamwise viscous force probability density function, $P(F_{v,x})$, is presented in Figure 6b. As in the pressure force distributions the spectrum of the barnacle-type topographies exhibits a wider range here as well. The peak of $P(F_{v,x})$ near $F_{v,x} \approx 0$ indicates local flow separation, while the enhanced $P(F_{v,x})$ values observed in the barnacle-type topographies show that these type of phenomena are stronger in such surfaces, as also shown in Figure 5c,d.

Summary and Conclusions

Direct numerical simulations were performed over spatially developing boundary layers covered by synthesized biofouling-type roughness comprised of both barnacle- and tubeworm-type organisms at a fixed planar and various frontal solidities. The results suggest that both the roughness function and the boundary layer growth, as well as the skin friction evolution scale with the frontal solidity for both barnacle- and tubeworm-type topographies. It is noted that the effect of frontal solidity to the mean flow becomes more dominant in the barnacle-type surfaces where other topographical parameters such as their proximity and their characteristic height, which is larger, play a crucial role. Overall, the individual organisms show local flow-separation patterns which are similar to well documented cases in the literature, such as isolated wall-mounted objects.

REFERENCES

Dehn, Christina, Holm, Eric, Chang, Peter, Vargas, Abel & Storms, Scott 2017 An approach for the scanning and construction of biofouled surfaces to be used for drag measurements. In *Proceedings of the 30-th American Towing Tank Conference*, pp. 1–14. West Bethesda, MD.

Kaminaris, Ioannis K., Balaras, Elias, Schultz, Michael P. & Holm, Eric R. 2023*a* Hydrodynamics of biofouling: Blending hull inspections to high-fidelity computations and experiments. *Proceedings of the 8th Hull Performance and Insight Conference (HullPIC) 2023, Pontignano, Italy, August 28-30* .

Kaminaris, Ioannis K., Balaras, Elias, Schultz, Michael P. &

Volino, Ralph J. 2023*b* Secondary flows in turbulent boundary layers developing over truncated cone surfaces. *Journal of Fluid Mechanics* **961**, A23.

MacDonald, M., Chan, L., Chung, D., Hutchins, N. & Ooi, A. 2016 Turbulent flow over transitionally rough surfaces with varying roughness densities. *Journal of Fluid Mechanics* **804**, 130–161.

Monty, J. P., Dogan, E., Hanson, R., Scardino, A. J., Ganapathisubramani, B. & Hutchins, N. 2016 An assessment of the ship drag penalty arising from light calcareous tubeworm fouling. *Biofouling* **32** (4), 451–464, pMID: 26958740.

Sarakinos, Sotirios & Busse, Angela 2022 Investigation of rough-wall turbulence over barnacle roughness with increasing solidity using direct numerical simulations. *Phys. Rev. Fluids* **7**, 064602.

Schultz, MP, Bendick, JA, Holm, ER & Hertel, WM 2011 Economic impact of biofouling on a naval surface ship. *Biofouling* **27** (1), 87–98.

Schultz, Michael P. 2007 Effects of coating roughness and biofouling on ship resistance and powering. *Biofouling* **23** (5), 331–341.

Womack, Kristofer M., Volino, Ralph J., Meneveau, Charles & Schultz, Michael P. 2022 Turbulent boundary layer flow over regularly and irregularly arranged truncated cone surfaces. *Journal of Fluid Mechanics* **933**, A38.

Yang, Jianming & Balaras, Elias 2006 An embedded-boundary formulation for large-eddy simulation of turbulent flows interacting with moving boundaries. *J. Comput. Phys* **215** (1), 12–40.